# Porous Boron-Doped Diamond/Carbon Nanotube Electrodes

H. Zanin,[*,†] P. W. May,[†] D. J. Fermin,[†] D. Plana,[†] S. M. C. Vieira,[‡] W. I. Milne,[‡] and E. J. Corat[§]

[†]School of Chemistry, University of Bristol, Bristol BS8 1TS, United Kingdom

[‡]Department of Engineering, University of Cambridge, 9 JJ Thomson Avenue, Cambridge CB3 0FA, United Kingdom

[§]National Institute for Space Research, Av. dos Astronautas 1758, São José dos Campos, São Paulo 12227-010, Brazil

**ABSTRACT:** Nanostructuring boron-doped diamond (BDD) films increases their sensitivity and performance when used as electrodes in electrochemical environments. We have developed a method to produce such nanostructured, porous electrodes by depositing BDD thin film onto a densely packed "forest" of vertically aligned multiwalled carbon nanotubes (CNTs). The CNTs had previously been exposed to a suspension of nanodiamond in methanol causing them to clump together into "teepee" or "honeycomb" structures. These nanostructured CNT/BDD composite electrodes have been extensively characterized by scanning electron microscopy, Raman spectroscopy, cyclic voltammetry, and electrochemical impedance spectroscopy. Not only do these electrodes possess the excellent, well-known characteristics associated with BDD (large potential window, chemical inertness, low background levels), but also they have electroactive areas and double-layer capacitance values ~450 times greater than those for the equivalent flat BDD electrodes.



**KEYWORDS:** *diamond, carbon nanotubes, porous electrodes, electrochemistry, high capacitance*
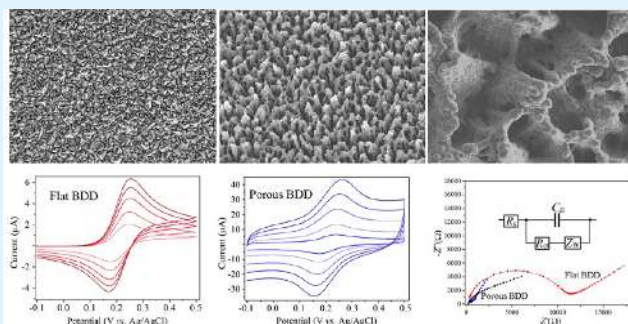
## ■ INTRODUCTION

The exceptional set of physical properties possessed by synthetic diamond films grown by chemical vapor deposition (CVD),[1] including extreme mechanical hardness, excellent thermal conductivity, and broad optical transparency from the deep ultraviolet to the far-infrared, have made them a material of considerable scientific interest in last few decades.[2,3] Although n-type doping remains problematic, p-type doping can be readily achieved by adding boron-containing gases into the CVD gas mixture during diamond growth.[4] The electrical conductivity of the diamond films can be altered from being highly insulating to near metallic by simply controlling the amount of boron added to the gas mixture. As well as finding application in electronics and sensors, such B-doped diamond (BDD) films are increasingly being used as electrodes in electrochemical redox cells.[5,6] This is because BDD electrodes have a number of advantages over conventional platinum or glassy carbon electrodes, including a wide potential window in aqueous media and a very low background current, in addition to chemical and physical stability.[7] Planar BDD electrodes, usually grown with a microcrystalline faceted morphology (as shown in Figure 1a), have found applications as sensitive detectors for redox-active compounds in water,[8] as biosensors,[9−11] and for water purification.[12] However, for optimal performance and sensitivity, either the electrode has to be miniaturized to make a microelectrode[13,14] or the surface area of the electrode needs to be as large as possible. Both approaches have their problems: microelectrodes are difficult to fabricate and handle, while large-area diamond substrates are

currently difficult and expensive to fabricate and not readily available commercially.

One solution to this problem is to grow the CVD diamond films onto a porous substrate material. The ideal substrate should have high porosity and be able to withstand the harsh CVD growth conditions and the compressive stresses that result from an overlying diamond film, as well as remain mechanically robust with good electrical conductivity. Moreover, the diamond film must be well adhered and cover the substrate surface conformally, without pinholes, while maintaining the large-area porous structure. With this in mind, porous silicon has been coated with diamond by a number of workers,[15−17] although the films suffered from weakened mechanical stability and poor electrical contacts between the Si and diamond. Porous titanium has also been used as a substrate for diamond growth;[18−20] however, the Ti reacts with the hydrogen present in the diamond CVD growth process increasing crack formation throughout the Ti bulk,[20] with subsequent reduction of mechanical stability.

An alternative method to prepare porous diamond films is to etch a dense matrix of holes into the diamond surface. Kriele et al.[21] annealed nanodiamond films at 550 °C in air for 1 h to selectively etch away the graphitic grain boundaries to produce diamond with varying degrees of porosity, while Shenderova et al.[22] reported nanostructured diamond honeycomb films
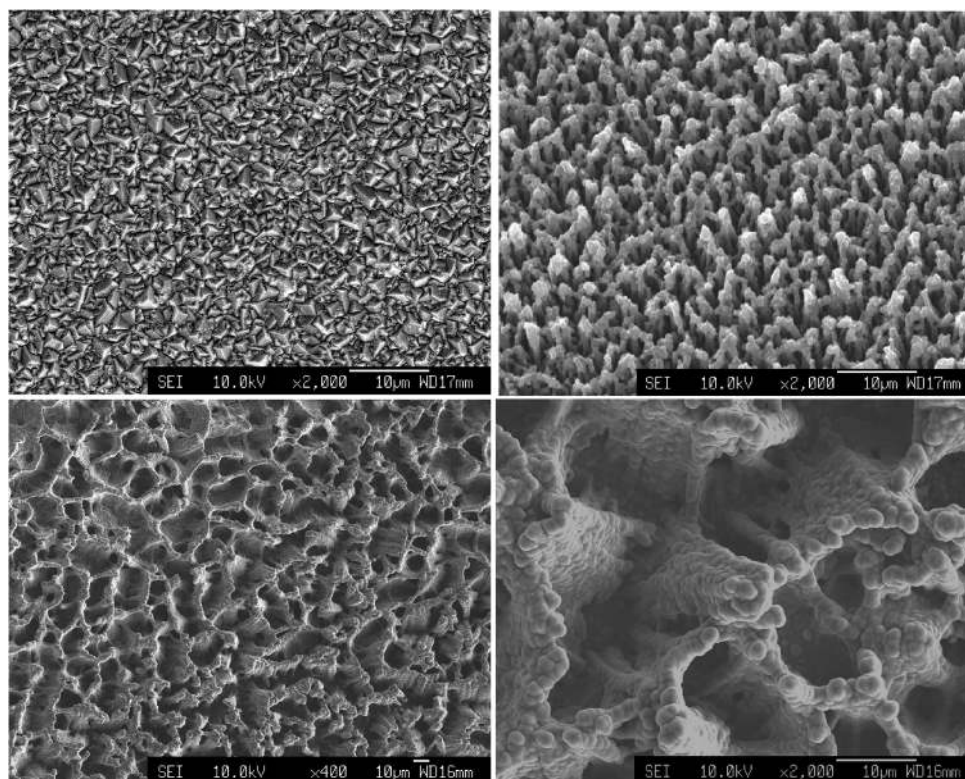
**Figure 1.** Electron micrograph images of the three types of BDD electrode under study: (a) microcrystalline flat diamond film, (b) CNT/BDD teepee matrix, (c) CNT/BDD ridged/honeycomb surface, and (d) higher magnification view of the film in (c).

prepared by etching through a porous anodic alumina mask. However, both these methods required freestanding BDD that was thick enough to withstand handling, which is difficult, expensive, and time-consuming to produce. To overcome this, Nebel et al.[23] reported that vertically aligned diamond nanowires could be produced by reactive ion etching (RIE) of a thin, flat BDD film through a micromask matrix made from nanodiamond particles. The diamond nanowires exhibited exceptionally sensitive electro- and biochemical sensitivity, demonstrating the high performance that can be achieved from diamond electrodes with large effective surface areas.

Another approach is to coat the diamond onto a suitably nanostructured substrate, and one of the cheapest and easiest methods to achieve this is to use vertically aligned carbon nanotubes (VACNTs). Diamond coating individual CNTs is possible but difficult;[24−26] however, the resulting CNT/ diamond "needles" are not very mechanically robust, and the amount of current that can be drawn from each needle is limited; at high currents the tips can rapidly erode away or the entire needle burn up. To get around this problem, we recently showed that dense "forests" of multiwall VACNTs can be connected together at their tips to form "teepee" structures by simply immersing the sample in liquid.[27] Electrospray seeding[28] of these VACNT forests with a nanodiamond suspension also produced teepees, which could be locked into position by coating with a thin CVD BDD layer. The number of CNTs joined together to form one teepee depended on the original areal density of the VACNTs and typically was around 20−100. Such teepee arrays proved to be excellent field emitters of electrons, with high current loads possible because the current was shared among so many CNT "legs", while the emitting surface was a rounded tip of BDD which did not easily burn out. Thus, these teepee structures combined the high electrical

conductivity of CNTs with the robust surface of diamond, leading to greatly extended lifetimes for field emission. In a later paper, we showed that similar results could be achieved by using a diamond-like carbon (DLC) coating to lock the clumped VACNTs into a 3D structure.[28] In this case, the areal density of the CNTs used was much greater than in the previous experiments, and so, rather than form teepees, they instead formed interconnected ridged structures, similar to distorted honeycombs. Although they were originally tested for field emission, both of these nanostructured materials, the teepees and honeycombs, consisted of a BDD or DLC surface with a very high surface area, which makes them ideal candidates for electrochemical electrodes.

In this work, we have investigated the use of these CNT/ BDD teepee structures as electrodes and have studied the effect of diamond crystallinity, CNT areal density, and substrate material upon the nanostructures formed and their electrochemical behavior. Of particular interest is the effective electrochemical area (as opposed to the geometrical area) of these structures, as this determines the sensitivity of the electrodes. We have also measured the capacitance of these layers to ascertain whether they might be suitable candidates for application in supercapacitor devices.

## ■ EXPERIMENTAL SECTION

Two types of VACNT forests were used to prepare different BDD nanostructures with varying porosity. The first type of VACNT was deposited and subsequently treated exactly as described in ref 28 to produce CNT/BDD teepees. Briefly, multiwalled CNTs were grown in a d.c.-plasma-enhanced CVD reactor on single-crystal Si (100) substrates seeded with Ni nanoparticle catalysts. This produced a VACNT forest with CNTs with length of ~5 $\mu$m, width of 20−50 nm, and areal density of ~1 × 10$^9$ cm$^{-2}$. These were then electrospray

seeded with a suspension of 5 nm detonation nanodiamond in methanol which caused the CNTs to clump into teepees, with each teepee consisting of ~20−40 CNTs joined at the top, with a teepee density of ~$10^7$ cm$^{-2}$. Subsequent short (1.5 h) diamond CVD was performed in a hot filament reactor using 1% CH$_4$/H$_2$ with diborane (B$_2$H$_6$) as a source of boron, causing the teepees to become coated with a thin (~0.5 $\mu$m) layer of BDD, as shown in Figure 1b. The gas-phase B concentration was sufficient to ensure that the diamond was heavily doped and therefore had near-metallic conductivity.

The second type of VACNT differed from the first in three respects: they were longer (40 $\mu$m), their areal density was much greater, and also they were deposited onto a conducting titanium substrate (as opposed to a poorly semiconducting Si substrate). To fabricate them, a 10 nm Ni layer was deposited on the Ti substrate by electron-beam evaporation and placed into a 2.45 GHz microwave (MW) plasma CVD chamber.[29] A plasma of N$_2$/H$_2$ (10/90 sccm) was used to heat the substrate, causing the thin Ni layer to ball up into nanoparticles that became the catalyst particles for subsequent VACNT growth in the same chamber. The length, diameter, and density of the CNTs could be varied by changing the growth conditions. For the CNTs reported here, CH$_4$ (14 sccm) was the process gas which was introduced into the chamber for 1 min, maintaining a substrate temperature of 800 °C and a reactor pressure of 30 Torr. This produced a VACNT forest with CNTs with length of 40 $\mu$m, width of 20−50 nm, and areal density of ~2.5 × $10^{10}$ cm$^{-2}$. Electrospray seeding followed by diamond CVD were then performed using the same conditions as before. Due to the higher CNT packing density, rather than forming teepees, these CNTs instead clumped together into long extended ridges or honeycombs, as shown in Figure 1c. A thin layer of BDD was deposited by CVD onto these structures using the same conditions as above, and the material morphologies are presented in Figure 1c,d. We estimate that each ridge contains 800−1200 CNTs, although this varies depending on the amount of lateral interconnection between ridges.

As a control sample, a BDD film was deposited onto a flat single-crystal (100) Si substrate (p$^+$, resistivity 0.01−0.02 $\Omega$ cm) using the same CVD conditions except for a deposition time of 7 h. This resulted in a continuous microcrystalline BDD film with a thickness of ~1−2 $\mu$m, with a surface morphology as shown in Figure 1a and typical grain size of ~1 $\mu$m.

The surface morphologies of the samples were imaged using a field emission scanning electron microscope (JEOL JSM-6330F) operating at an accelerating voltage of 10 kV and a beam current of 12 $\mu$A. Laser Raman spectra (Renishaw) were recorded at room temperature with UV laser excitation (325 nm).

The three types of diamond sample (which we shall henceforth refer to as teepees, honeycombs, and a flat control sample) were mounted as electrodes and characterized by cyclic voltammetry (CV) and electrochemical impedance spectroscopy (EIS). The electrical contact of the working electrodes was performed through the diamond surface using silver paint and copper wire and insulated using Teflon tape. A standard three-electrode cell system was set up to evaluate the room-temperature electrochemical performance of the electrodes in a potentiostat (AutolabPGSTAT30). High-purity platinum wire and Ag/AgCl (3 mol dm$^{-3}$) were employed as counter electrodes and reference electrodes, respectively. All potentials are quoted relative to this reference. All electrochemical experiments were carried out exposing a constant geometric area of 7.07 mm$^2$ (3 mm diameter) of the working electrode.

Three different aqueous electrolyte solutions were used to evaluate different aspects of the electrochemical performance using two redox species, where potassium nitrate (KNO$_3$) was the electrolyte support. The redox species come from ferrocene−methanol (C$_{11}$H$_{12}$FeO), potassium ferrocyanide K$_3$[Fe(CN)$_6$], and ferrocyanide (K$_4$[Fe(CN)$_6$]), which were obtained from Aldrich and used without further purification. The CV measurements were carried out using scan rates of 0.010−0.1 V s$^{-1}$ at potentials of −0.1 to 0.5 V. Prior to taking the CV measurements, a pretreatment was performed in which the system was held at −0.1 V for 1 min to polarize the electrodes, and then, a

first scan was taken from −0.1 V in the oxidation direction for each sample.

Impedance spectroscopy measurements were carried out at the formal redox potential of the corresponding probe within the frequency range of 0.1 to 1000 Hz and amplitude of 5 mV rms. At the end of each measurement, the Kramers−Kronig test[30] was applied to evaluate the consistency (causality, linearity, and stability) of the EIS data. Modified Randles circuits were employed in order to fit the impedance spectra obtained.

## ■ RESULTS

Figure 1 shows SEM micrographs of the typical morphology of the three types of BDD electrode under study, while Figure 2
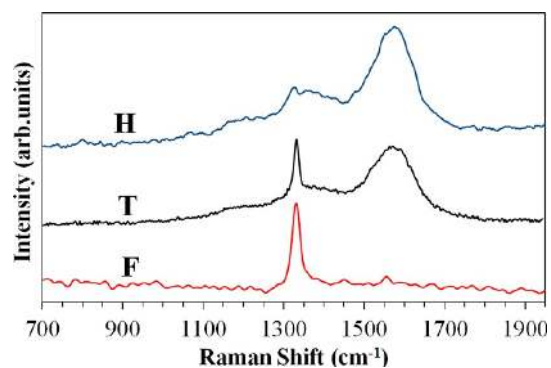


**Figure 2.** Laser Raman spectra of flat (F), teepee (T), and honeycomb (H) BDD electrodes using 325 nm laser excitation. The spectra have been offset vertically for clarity.

shows the corresponding laser Raman spectra which are consistent with the films being microcrystalline diamond.[31] The Raman spectra from the diamond-coated CNTs reveals the sp$^3$ diamond peak at 1332 cm$^{-1}$, the D and G bands due to disordered and ordered sp$^2$ carbon at around 1350 and 1550−1600 cm$^{-1}$, respectively, and the peak at around 1120−1180 cm$^{-1}$ due to sp$^2$ carbon at the grain boundaries of nanocrystals.[32]

Figure 3 presents the cyclic voltammograms obtained from the three different aqueous solutions at a scan-rate of 0.01 V s$^{-1}$. In Figure 3a, the voltammograms from the nanostructured BDD electrodes in KNO$_3$ have a "quasi-rectangular" shape, which is typical of interfacial double-layer (DL) charging.[33,34] The DL charging current is proportional to the real surface area of the electrode. There is significant difference in the capacitive current of the two nanostructured BDD electrodes compared with that from the flat sample. This is not surprising, as DL charging is most apparent in systems with a large surface-area-to-volume ratio, such as in materials with pores or structures on the scale of $\mu$m to nm.[35] Here, both the teepee and honeycomb samples have 3D structures on this length scale. From the relative areas inside the CV plots, the honeycomb sample has the higher capacitance and, hence, the larger electroactive surface area,[36,37] possibly due to the longer carbon nanotubes used in its preparation and their higher real density area. Compared to the voltammogram from the nanostructured BDD electrodes, the voltammogram from the conventional flat BDD electrode looks like a horizontal line, indicating a significantly lower specific surface area.[38,39]

The electrochemical properties of the nanostructured CNT template BDD electrodes were investigated by cyclic voltammetry of outer-sphere redox probes.[40] Figure 3b,c compares the voltammetric responses of the three BDD
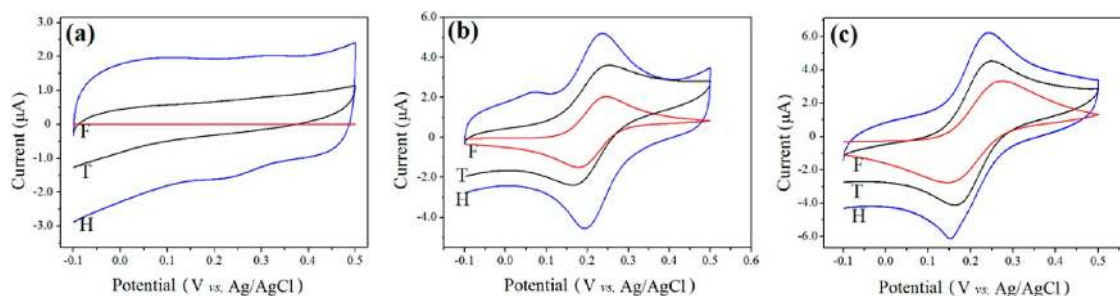
**Figure 3.** Comparison of cyclic voltammetry curves of (a) 0.1 M potassium nitrate electrolyte; (b) 0.5 mM ferrocene−methanol in 0.1 M potassium nitrate; and (c) 1 mM ferri/ferrocyanide in 0.1 M potassium nitrate, for the three types of BDD electrodes (flat (F), teepee (T), and honeycomb (H)), all taken at a constant 0.01 V s$^{-1}$ scan rate.
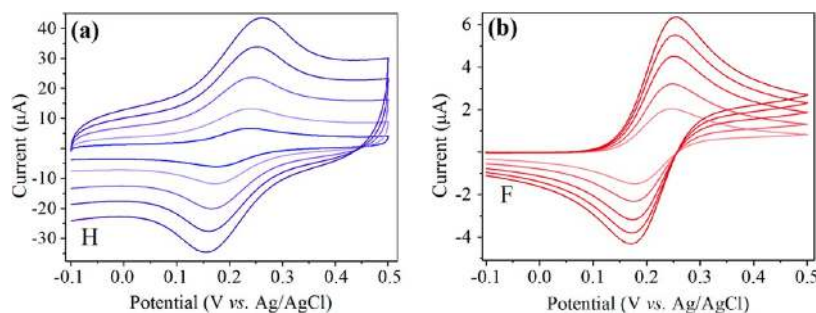


**Figure 4.** CV responses obtained using (a) honeycomb (H) and (b) flat (F) BDD electrodes for the ferri/ferrocyanide redox reaction taken at different scan rates (0.010, 0.025, 0.050, 0.075, and 0.1 V s$^{-1}$).

electrodes when oxidizing and reducing (b) 0.5 mM of ferrocene−methanol and (c) 0.5 mM of ferricyanide and 0.5 mM of ferrocyanide as a redox couple. The oxidation and reduction peaks are clearly defined in both solutions (∼0.24 and 0.18 V, respectively, for ferrocene−methanol and ∼0.25 and 0.17 V, respectively, for ferri/ferrocyanide) while the effect of the DL charging on the CV area is also apparent.

Figure 4 shows the voltammetric responses of the (a) honeycomb and (b) flat BDD electrodes for the solution of 0.5 mM of ferri/ferrocyanide, varying the scan rate from 0.01 to 0.1 V s$^{-1}$. A significant difference in the peak currents of ∼1 order of magnitude higher can be observed for the honeycomb electrode compared to the flat electrode, reflecting the increased charging (background) current. The oxidation and reduction peaks remain at almost the same potential independent of scan rate, with a constant separation of 0.059 V, indicative of a reversible redox process.[41]

Electrochemical impedance analyses were performed on the three BDD electrodes in aqueous solutions containing KNO$_3$ as the supporting electrolyte. These data were taken at the formal potential for each electrode and redox solution. Figure 5a−d shows a comparison of impedance spectra for each of the three BDD electrodes and for both redox-active solutions, presented as: (a,b) Nyquist plots and (c,d) Bode plots. The Bode plots show that for both solutions the impedance decreased markedly on going from the flat substrate to the nanostructured ones. The honeycomb sample showed slightly lower impedance amplitude than the teepee sample, as a result of the larger double layer capacitance.

The impedance spectra were fitted to the Randles equivalent circuit[42] (inset in Figure 5b), which models the electrochemical electrode as an active electrolyte resistance $R_s$ and is in parallel with a combination of the double-layer capacitance, $C_{dl}$, and the impedance of the faradaic reaction, called the Warburg

impedance, $Z_W$,[43−45] together with the charge-transfer impedance ($R_{ct}$). $R_s$ is the internal resistance of the system, which consists of the ionic resistance of the electrolyte, the intrinsic resistance of the active material, and the contact resistance at the electroactive material/current collector interface.[46] $Z_W$ represents the mass transport impedance and is related to the rate of diffusion to and from the electrode by redox species.[47] Because the electrode surface is not perfectly smooth and infinitely large, it will not behave like a perfect capacitor, and charging of the electrical double layer will be nonfaradaic. The standard way to account for the microscopic roughness and atomic-scale inhomogeneity in the surface is to replace $C_{dl}$ with a constant phase element, CPE, given by CPE $= Q^{1/n}$ with $Q$ being the charge and $n > 0.9$. Thus, CPE is the effective capacitance of the double layer for nanostructured electrodes.

The impedance data were fitted using the Autolab FRA software using $R_s$, $C_{dl}$, $Z_W$, and $R_{ct}$ as fitting parameters, and the results are shown as the full lines in Figure 5a,b, while the extracted data are tabulated in Table 1. The $R_s$ value is independent of the redox couple and remains constant at ∼0.25 ± (0.08), 0.23 ± (0.07), and 0.21 ± (0.05) kΩ for honeycomb electrodes. The $Z_W$ values are 0.11 ± (0.05) 10$^{-3}$ for ferrocene−methanol and 0.21 ± (0.07) 10$^{-3}$ for ferri/ferrocyanide solutions. The values for $R_{ct}$ and CPE are surface dependent, with the honeycomb sample having the lower impedance and higher capacitance in all measurements, which is consistent with the findings from the CVs. Indeed, the striking aspect of these results is the very large values for the capacitance of the nanostructured films, which are 150−450 times greater than for the conventional flat electrode. Using these capacitance ratios, together with the known geometric area for the flat electrode (7.07 mm$^2$), the electroactive surface areas of the two nanostructured BDD electrodes were
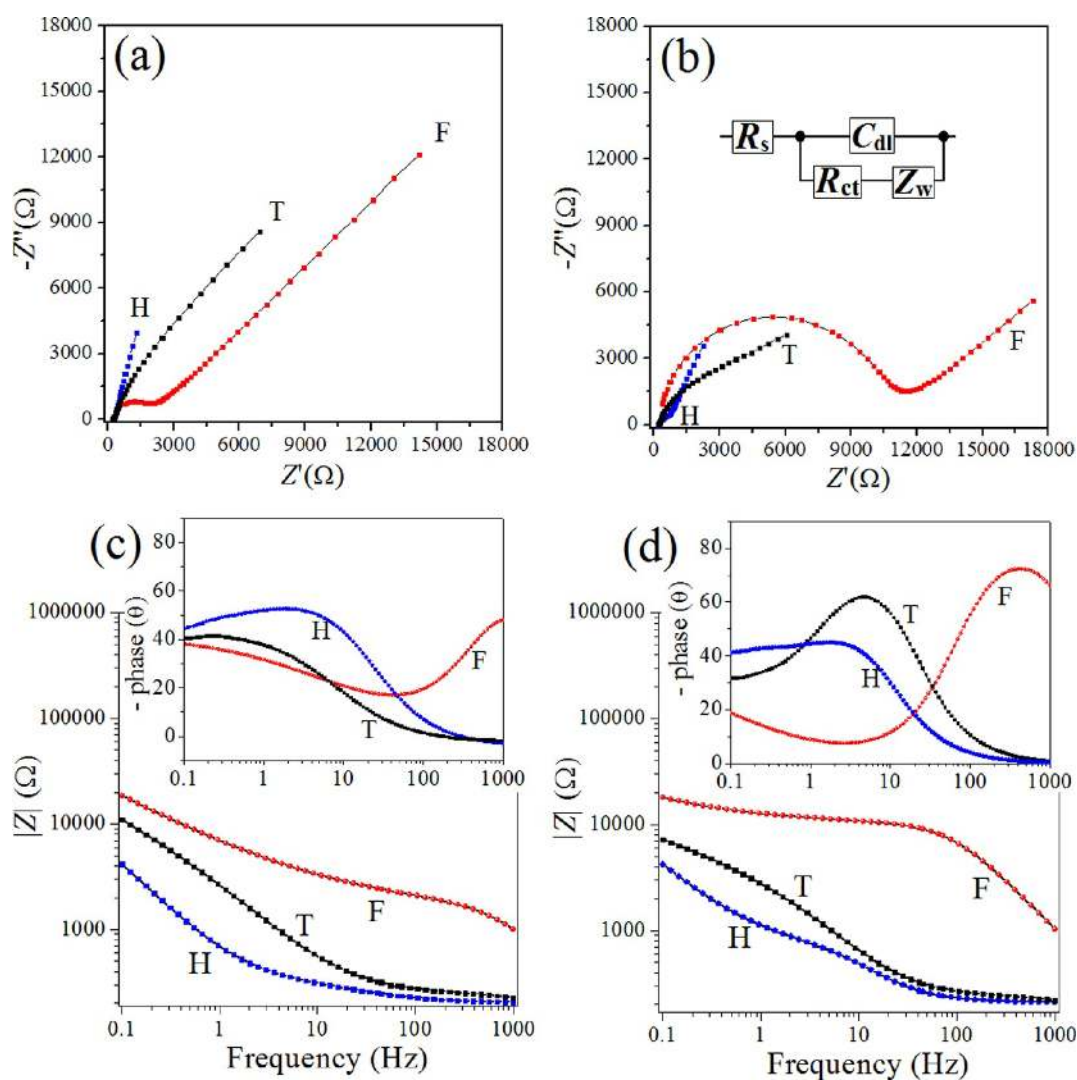
**Figure 5.** Impedance spectra taken at the formal potential as the frequency is increased from 0.1 to 1000 Hz for the three BDD electrodes in the two redox systems: (a,c) 0.5 mM ferrocene−methanol; (b,d) 1 mM ferri/ferrocyanide solution. (a,b) are presented as Nyquist plots, i.e., the real component of impedance, $Z'$, against the imaginary component of the impedance, $Z''$, with the full lines being the best-fit to the modified Randles equivalent circuit model, shown as an inset into (b). $R_s$ is the resistance of the system; $R_{ct}$ is the charge-transfer resistance; $C_{dl}$ is the capacitance of the charged double-layer at the BDD electrode surface; and $Z_W$ is the Warburg impedance. (c,d) are presented as Bode plots, i.e., the modulus of the impedance, $|Z|$, against the frequency. Inset: phase of the impedance responses.

**Table 1. BDD Electrode Properties Extracted from Fitting the Nyquist Plots in Figure 5a,b**

| | 0.5 mM $C_{11}H_{12}FeO$ | | 0.5 mM $K_4[Fe(CN)_6]$ 0.5 mM $K_3[Fe(CN)_6]$ | |
| --- | --- | --- | --- | --- |
| samples | CPE ($\mu F$) | $R_{ct}$ (k$\Omega$) | CPE ($\mu F$) | $R_{ct}$ (k$\Omega$) |
| flat | 0.23 ± (0.09) | 1.65 ± (0.05) | 0.24 ± (0.07) | 10.1 ± (0.6) |
| teepee | 36.4 ± (0.3) | | 36.9 ± (0.5) | 2.95 ± (0.07) |
| honeycomb | 104.5 ± (0.5) | | 105.6 ± (0.8) | 0.49 ± (0.09) |

estimated as ∼1100 mm² for the teepees and ∼3200 mm² for the honeycomb samples, which are consistent with the SEM images in Figure 1.

## ■ CONCLUSIONS

We have described a novel method to produce electrodes with large, electroactive surface areas, by depositing a thin layer of boron-doped diamond onto dense forests of vertically aligned carbon nanotubes. The size, shape, and porosity of the resulting nanostructured diamond/CNT composites can be controlled by changing the CNT length and areal density, as well as the

preparation method. Nanostructured diamond/CNT electrodes combine many of the advantages of CNTs (high conductivity, huge surface area) with the robust, inert surface of diamond, making them an excellent material for electrochemical electrodes. Such nanostructured composites have surface areas up to 450 times greater than conventional flat electrodes, which should greatly improve their sensitivity for detection of trace amounts of redox species, although this has yet to be tested. The capacitance of these nanostructured electrodes is also extremely large, being 150−450 times greater than the

equivalent flat electrodes. This suggests possible applications as supercapacitors and (bio) sensors.

In this study, 2 types of BDD/CNT composite structures were investigated, neither of which have yet been optimized for surface area or performance. The finding that electroactive surface area and effective capacitance depend strongly upon CNT length and density suggests that further improvements to these properties could be achieved by simply using denser CNT forests with longer CNTs, both of which are now readily commercially available over wafer-scale substrates. This may provide a route for low cost, very large area diamond/CNT electrodes for a plethora of electrochemical applications.

## ■ AUTHOR INFORMATION

**Corresponding Author**
*E-mail: hudson.zanin@bristol.ac.uk. Phone + 44 (0)117 928 7645.

**Notes**
The authors declare no competing financial interest.

## ■ REFERENCES

(1) May, P. W. *Philos. Trans. R. Soc., A: Math. Phys. Eng. Sci.* **2000**, *358*, 473−495.

(2) May, P. W. *Science* **2008**, *319*, 1490−1491.

(3) Balmer, R. S.; Friel, I.; Woollard, S. M.; Wort, C. J. H.; Scarsbrook, G. A.; Coe, S. E.; El-Hajj, H.; Kaiser, A.; Denisenko, A.; Kohn, E.; Isberg, J. *Philos. Trans. R. Soc., A: Math. Phys. Eng. Sci.* **2008**, *366*, 251−265.

(4) Mankelevich, Y. A.; Ashfold, M. N. R.; Comerford, D. W.; Ma, J.; Richley, J. C. *Thin Solid Films* **2011**, *519*, 4421−4425.

(5) Hupert, M.; Muck, A.; Wang, J.; Stotter, J.; Cvackova, Z.; Haymond, S.; Show, Y.; Swain, G. M. *Diamond Relat. Mater.* **2003**, *12*, 1940−1949.

(6) Kraft, A. *Int. J. Electrochem. Science* **2007**, *2*, 355−385.

(7) Swain, G. M.; Ramesham, R. *Anal. Chem.* **1993**, *65*, 345−351.

(8) Lete, C.; Teodorescu, F.; Marina, M. *Rev.Chim.* **2013**, *64*, 540−544.

(9) Nebel, C. E.; Rezek, B.; Shin, D.; Uetsuka, H.; Yang, N. *J. Phys. D: Appl. Phys.* **2007**, *40*, 6443−6466.

(10) Suzuki, A.; Ivandini, T. A.; Yoshimi, K.; Fujishima, A.; Oyama, G.; Nakazato, T.; Hattori, N.; Kitazawa, S.; Einaga, Y. *Anal. Chem.* **2007**, *79*, 8608−8615.

(11) Teofilo, R. F.; Ceragioli, H. J.; Peterlevitz, A. C.; Da Silva, L. M.; Damos, F. S.; Ferreira, M. M. C.; Baranauskas, V.; Kubota, L. T. *J. Solid State Electrochem.* **2007**, *11*, 1449−1457.

(12) Zanin, H.; Teofilo, R. F.; Peterlevitz, A. C.; Oliveira, U.; de Paiva, J. C.; Ceragioli, H. J.; Reis, E. L.; Baranauskas, V. *J. Appl. Electrochem.* **2013**, *43*, 323−330.

(13) Hu, J.; Holt, K. B.; Foord, J. S. *Anal. Chem.* **2009**, *81*, 5663−5670.

(14) Campbell, F. W.; Belding, S. R.; Compton, R. G. *ChemPhysChem* **2010**, *11*, 2820−2824.

(15) Baranauskas, V.; Chang, D. C.; Li, B. B.; Peterlevitz, A. C.; Trava-Airoldi, V. J.; Corat, E. J.; Singh, R. K.; Lee, D. G. *J. Porous Mater.* **2000**, *7*, 401−404.

(16) Khan, M. A.; Haque, M. S.; Naseem, H. A.; Brown, W. D.; Malshe, A. P. *Thin Solid Films* **1998**, *332*, 93−97.

(17) Baranauskas, V.; Li, B. B.; Peterlevitz, A. C.; Tosin, M. C.; Durrant, S. F. *Thin Solid Films* **1999**, *355*, 233−238.

(18) Sun, J.; Lu, H.; Lin, H.; Huang, W.; Li, H.; Lu, J.; Cui, T. *Mater. Lett.* **2012**, *83*, 112−114.

(19) Braga, N. A.; Cairo, C. A. A.; Almeida, E. C.; Baldan, M. R.; Ferreira, N. G. *Diamond Relat. Mater.* **2008**, *17*, 1891−1896.

(20) Braga, N. A.; Cairo, C. A. A.; Matsushima, J. T.; Baldan, M. R.; Ferreira, N. G. *J. Solid State Electrochem.* **2010**, *14*, 313−321.

(21) Kriele, A.; Williams, O. A.; Wolfer, M.; Hees, J. J.; Smirnov, W.; Nebel, C. E. *Phys. Lett.* **2011**, *507*, 253−259.

(22) Shenderova, O. A.; Padgett, C. W.; Hu, Z.; Brenner, D. W. *J. Vac. Sci. Technol., B* **2005**, *23*, 2457−2464.

(23) Nebel, C. E.; Yang, N.; Uetsuka, H.; Osawa, E.; Tokuda, N.; Williams, O. *Diamond Relat. Mater.* **2009**, *18*, 910−917.

(24) Shankar, N.; Glumac, N. G.; Yu, M.-F.; Vanka, S. P. *Diamond Relat. Mater.* **2008**, *17* (1), 79−83.

(25) Terranova, M. L.; Orlanducci, S.; Fiori, A.; Tamburri, E.; Sessa, V.; Rossi, M.; Barnard, A. S. *Chem. Mater.* **2005**, *17*, 3214−3220.

(26) Rosolen, J. M.; Tronto, S.; Marchesin, M. S.; Almeida, E. C.; Ferreira, N. G.; Poa, C. H. P.; Silva, S. R. P. *Appl. Phys. Lett.* **2006**, *88* (8), 083116.

(27) Zou, Y.; May, P. W.; Vieira, S. M. C.; Fox, N. A. *J. Appl. Phys.* **2012**, *112* (4), 044903.

(28) Zanin, H.; May, P.; Hamanaka, M. H. O. M.; Corat, E. J. *ACS Appl. Mater. Interfaces* **2013**, *5*, 12238−12243.

(29) Zanin, H.; Saito, E.; Ceragioli, H. J.; Baranauskas, V.; Corat, E. J. *Mater. Res. Bull.* **2014**, *49*, 487−493.

(30) Boukamp, B. A. *J. Electrochem. Soc.* **1995**, *142*, 1885−1894.

(31) Filik, J.; Harvey, J. N.; Allan, N. L.; May, P. W.; Dahl, J. E. P.; Liu, S.; Carlson, R. M. K. *Phys. Rev. B* **2006**, *74*, 035423.

(32) Zanin, H.; Peterlevitz, A. C.; Ceragioli, H. J.; Rodrigues, A. A.; Belangero, W. D.; Baranauskas, V. *Mater. Sci. Eng. C: Mater. Biol. Appl.* **2012**, *32*, 2340−2343.

(33) He, X.; Lei, J.; Geng, Y.; Zhang, X.; Wu, M.; Zheng, M. *J. Phys. Chem. Solids* **2009**, *70*, 738−744.

(34) Zhang, W.; Huang, Z.-H.; Cao, G.; Kang, F.; Yang, Y. *J. Power Sources* **2012**, *204*, 230−235.

(35) Xia, K.; Gao, Q.; Jiang, J.; Hu, J. *Carbon* **2008**, *46*, 1718−1726.

(36) Fuertes, A. B.; Pico, F.; Rojo, J. M. *J. Power Sources* **2004**, *133*, 329−336.

(37) Portet, C.; Taberna, P. L.; Simon, P.; Flahaut, E. *J. Power Sources* **2005**, *139*, 371−378.

(38) Waldvogel, S. R.; Elsler, B. *Electrochim. Acta* **2012**, *82*, 434−443.

(39) Zanin, H.; Peterlevitz, A. C.; Ceragioli, H. J.; Teofilo, R. F.; Degasperi, F. T.; Baranauskas, V. *ECS J. Solid State Sci. Technol.* **2012**, *1*, N67−N72.

(40) Bharathi, S.; Nogami, M.; Ikeda, S. *Langmuir* **2001**, *17*, 1−4.

(41) Granger, M. C.; Swain, G. M. *J. Electrochem. Soc.* **1999**, *146*, 4551−4558.

(42) Silva, T. A. *Electrochim. Acta* **2013**, in press; DOI: 10.1016/j.electacta.2013.12.024.

(43) Sakharova, A.; Nyikos, L.; Pleskov, Y. *Electrochim. Acta* **1992**, *37*, 973−978.

(44) Hernando, J.; Lud, S. Q.; Bruno, P.; Gruen, D. M.; Stutzmann, M.; Garrido, J. A. *Electrochim. Acta* **2009**, *54*, 1909−1915.

(45) Prabaharan, S. R. S.; Vimala, R.; Zainal, Z. *J. Power Sources* **2006**, *161*, 730−736.

(46) Bo, Z.; Wen, Z.; Kim, H.; Lu, G.; Yu, K.; Chen, J. *Carbon* **2012**, *50*, 4379−4387.

(47) Hwang, S.; Lee, B. S.; Chi, Y. S.; Kwak, J.; Choi, I. S.; Lee, S.-G. *Electrochim. Acta* **2008**, *53*, 2630−2636.